ACS APPLIED ELECTRONIC MATERIALS

pubs.acs.org/acsaelm

Article

Microfluidic Electronic Tongues Based on High-Entropy Nitride Films

Leonardo M. Leidens,* Carla D. Boeira, Maria H. Gonçalves, Endel E. C. Costa, María C. Marchi, Antonio R. Zanatta, Fernando Alvarez, and Antonio Riul, Jr.*

Cite This: ACS Appl. Electron. Mater. 2025, 7, 5537−5548

Read Online

ACCESS | Metrics & More | Article Recommendations | Supporting Information

ABSTRACT: High-entropy nitrides (HENs) are emerging as promising materials for sensing applications due to their exceptional chemical stability, diverse electrical properties, and highly tunable surface and bulk characteristics. This study integrates HEN thin films, deposited via RF sputtering, into an impedimetric microfluidic electronic tongue (e-tongue), designed to assess their potential for high sensitivity and robust detection of various analytes. The active films displayed a distinct oxide-rich surface and nitride-rich sublayer, directly influencing sensor performance. As a proof-of-concept, the unique electrical response of the HEN-based e-tongue enabled precise discrimination between similar ions (Na^+ and K^+) and basic human tastes (sweet, salty, bitter, umami, and sour) at concentrations near or below the human palatability threshold. Moreover, after repeated use, the films maintained their chemical and structural integrity, ensuring long-term stability and reproducibility. These results highlight the potential of HENs as versatile materials for advanced sensing applications, demonstrating their promise for next-generation e-tongue systems and expanding the range of applications for this class of materials.

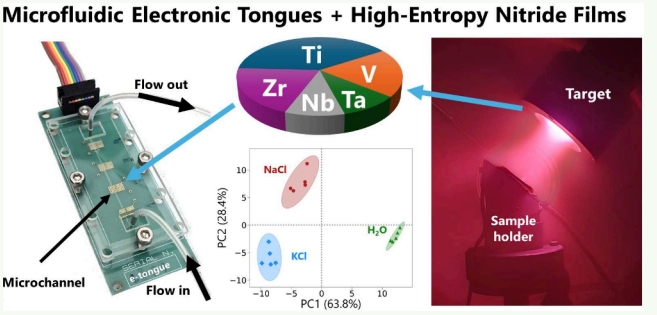

KEYWORDS: *high-entropy nitrides, e-tongue device, advanced sensors, thin film, sputtering*

1. INTRODUCTION

The growing demand for high-precision detection technologies drives advances in sensor development. Among these, electronic tongues (e-tongues) have emerged as versatile tools for applications ranging from food analysis to environmental monitoring.[1] According to the International Union of Pure and Applied Chemistry (IUPAC),[2] an e-tongue is defined as a "*multisensor system, which consists of a number of low-selective sensors and uses advanced mathematical procedures for signal processing based on the pattern recognition (PARC) and/or multivariate analysis [artificial neural networks (ANNs), principal component analysis (PCA)], etc.*" Unlike specific sensors, e-tongues use arrays of sensors to identify patterns,[3] and a new frontier is expanding in this type of sensing with the advancement of new materials and powerful computational tools. The former is applied to improve interactions with the systems of interest and the latter to analyze large amounts of information, such as multivariate analysis (MVA) and statistical techniques for identifying patterns and variable correlations in complex multivariate systems.[1,4]

The tongue and taste perception inspired the acronym e-tongue.[5] When a human tastes a flavor, taste buds in the tongue do not individually identify each chemical compound of the substance being savored; instead, they provide a flood of information to the brain, which ends up identifying it in a comprehensive "fingerprint" of the taste.[1,5−7] This ability is called global selectivity and uses the combinatorial response of nervous stimuli. Indeed, flavor receptors in *taste buds* are not fully selective for just one type of molecule; instead, several receptors respond to the stimulus, and the neural networks in the brain generate a unique response pattern that is easily recognized. An e-tongue device tries to mimic this natural process instead of individually detecting each compound in a solution. Still, it provides a global response pattern representing the "fingerprint" of the liquid under analysis, e.g., from aqueous solutions to synthetic blood or saliva.[8] Here, this effect is emulated with arrays of interdigitated electrodes (IDEs) properly coated by thin films that alter the electrical response of bare IDEs, a key condition for sample discrimination.[1]

e-Tongues are currently applied in several areas.[2,9−13] Briefly, some are used in the food and beverage industry for taste analysis, adulterations, and quality control.[14−18] In the environmental domain,[19] e-tongues play a role in monitoring pollutants in water and detecting compounds in effluent waste.[20] Additionally, this technology is emerging in the

Received: March 11, 2025
Revised: May 22, 2025
Accepted: May 24, 2025
Published: June 5, 2025

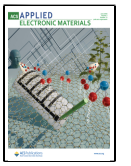

pharmaceutical industry to assess drug formulations,[21] evaluate taste masking,[22] and analyze biological fluids to identify biomarkers for diseases.[23,24] More recently, bioelectronic and plasmonic tongues are expanding the realm of advanced sensing using similar concepts.[25−27] Despite their success, challenges related to stability, chemical degradation, and limited mechanical robustness of the sensing films persist, particularly under harsh environmental conditions or prolonged operation.[28] Traditional impedimetric e-tongues typically employ polymer-based films, often fabricated by the layer-by-layer (LBL) technique,[29] deposited onto IDEs to form sensing units of the device.[30] However, polymeric films can suffer from delamination, swelling, and chemical deterioration when exposed to aggressive analytes or extended cycling, limiting device lifetime and reliability.[31] In this context, there is strong motivation to explore novel material systems capable of enhancing mechanical durability, chemical resistance, and operational stability. High-entropy nitride (HEN) coatings offer a promising alternative, combining the chemical versatility required for differential sensing with superior mechanical properties and environmental resilience, thereby expanding the potential application range of electronic tongue devices.

In the past decades, high-entropy materials have formed an emerging class of advanced materials offering promising solutions due to unique thermal, chemical, and mechanical stability and tunable properties.[32,33] Along with the polycrystalline solid solution metallic alloys[34] and amorphous metallic glass form,[35] the high-entropy ceramics,[36] formed by high-entropy oxides (HEOs)[37] and high-entropy nitrides (HENs)[38] and, more recently, high-entropy borides, have been developed for solar energy applications.[39] The HEN's subclass comprises five or more metals in near-equimolar ratios and nitrogen, forming a disordered, solid solution phase with simple crystalline structures, such as a NaCl crystallographic face-centered cubic (*fcc*) arrangement.[40] The main properties of such advanced ceramic metals include superior thermal, corrosion, and wear robustness compared to the single nitrides formed by the alloy's elements individually.[41] HEN films have already demonstrated potential across various fields, despite their relative novelty. In aerospace parts, they can be used to protect components from extreme temperatures and mechanical wear.[42] In machining applications, they may enhance durability.[43] In biomedicine,[44] they are investigated for implants due to their corrosion resistance and biocompatibility. In electronics, they act as diffusion barriers in semiconductor devices.[45] Combining these properties, their chemical stability makes this class of materials ideal for applications in harsh environments such as industrial process monitoring and precision agriculture.

Physical vapor deposition (PVD) is a highly effective technique for synthesizing these materials on different substrates, producing uniform thin films with excellent compositional and thickness control.[40,46] Moreover, it is a well-studied, environmentally friendly technique, avoiding waste or chemical inputs to deposit the coatings. A key advantage of PVD is the ability to tailor HEN properties by adjusting deposition parameters such as substrate temperature, pressure, gas composition, and target material.[47] For instance, substrate temperature influences grain size and surface roughness, while chamber pressure affects the stoichiometry and layer density. Recent advances, such as Dynamic Glancing Angle Deposition (DGLAD), further refine micro- and nanostructures by oscillating the substrate during deposition.[48] This flexibility allows optimized films for specific applications, supporting industrial-scale production and, in particular, expanding the potential use of sensor technologies.

The interest of the present study is the potential alignment with e-tongue sensor technology positioning HEN films as transformative solutions for overcoming the limitations of conventional materials. Specifically, it is possible to form materials with distinct electrical features by tuning the deposition parameters. Moreover, several combinations of metallic nitrides that constitute the thin films of the e-tongue enhance the electrical response of the gadget. In this context, we explore here how incorporating HENs into IDEs can modulate the response of the sensing units, while enhancing electrical response, robustness, and stability. The compositional diversity of HENs enables property customization to meet specific application needs, while PVD ensures reproducibility, which is essential for the technological scalability. We detail the preparation of three distinct HEN thin films deposited onto IDEs, ensuring the device integrity. By characterizing the chemical and electrical properties of these films, we assess their impact on sensor performance, stability, and applications in potential scenarios. This study advances state-of-the-art e-tongues, demonstrating proof-of-concept for a HEN-enhanced e-tongue, while showcasing how interdisciplinarity among materials science, analytical chemistry, and surface engineering can drive innovations in detection sensor technologies, combining advanced material science employing modern statistical analysis. Indeed, the paper shows the power of treating large amounts of experimental data obtained by e-tongue devices by using multivariate analysis tools, identifying patterns and variable correlation in a multivariable complex system.

2. MATERIALS AND METHODS

2.1. High Entropy Nitride (HEN) Thin Film Deposition. The deposition of the studied samples is carried out using a custom-built Multipurpose Thin Films Equipment, which consists of a vacuum chamber equipped with a 2 in. diameter, water-cooled magnetron sputtering source (ST20, AJA International), operated by an RF power supply (Lesker R301 generator − 13.56 MHz, 300 W, with an automatic matching network - MC2). An RF power supply was selected due to its ability to maintain stable plasma conditions even when working with partially insulating targets or films, as is common during nitride formation. RF sputtering also offers robust control over gas composition, ion energy, and film growth parameters, enabling the deposition of high-quality films at relatively low substrate temperatures, which is a critical factor for integrating the coatings into microfabricated substrates and microfluidic devices without inducing thermal damage. Although other techniques, such as direct current (DC) sputtering[49] and high-power impulse magnetron sputtering (HiPIMS),[50] have also been reported for the synthesis of HEN thin films, RF sputtering provided an optimal balance between process stability, film uniformity, and compatibility with our fabrication constraints.

The multicomponent sputtering target consists of a 5-element (NbTaTiVZr) assembly of transition metals arranged in a circular, "pizza-shaped" geometry (Figure 1). Due to the different components' sputtering yields, the area of each element is optimized in previous studies[51,52] to ensure a near-equimolar composition of the metals in the films, as required for high-entropy materials. After optimization, the target is formed of approximately 40% Ti, 20% V, 20% Zr, 10% Ta, and 10% Nb by the area fraction. In this study, the distance between the sputtering target and the substrate was fixed at approximately 6 cm.

https://doi.org/10.1021/acsaelm.5c00489
ACS Appl. Electron. Mater. 2025, 7, 5537−5548

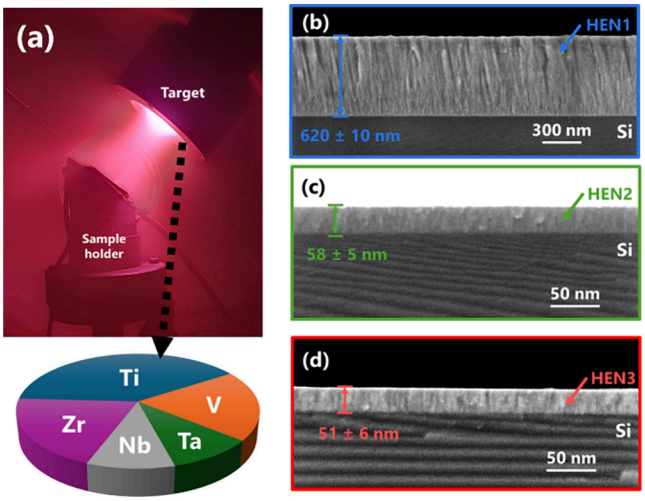

Figure 1. Photograph of the deposition processes is presented in (a) as well as a schematic of the pizza-shaped target used to deposit the HEN films. Subfigures (b), (c), and (d) show, respectively, the cross sections of HEN-1, HEN-2, and HEN-3 films.

The sample holder is modified to enable variation of the substrate angle during deposition in the Dynamic Glancing Angle Deposition (DGLAD) configuration.[48] The chamber was evacuated to a pressure of $<1.5 \times 10^{-4}$ Pa before deposition. The sputtering target is cleaned before deposition using argon plasma etching at a working pressure of ∼0.9 Pa and a power of 150 W from the RF source, with the substrates properly masked by a shutter. During deposition, the substrates were not subjected to any external bias. However, the surface develops a floating potential estimated at approximately −14 V under the plasma conditions employed (the detailed calculation is provided in the Supporting Information file).

Three films are produced under different conditions, initially on Si (100) substrates, and later optimized on printed circuit boards (PCBs) containing the IDE electrodes. The e-tongue device consists of four gold interdigitated electrodes (IDEs) in a polymeric printed circuit board (PCB). The IDEs have four pairs of digits with a 5 mm length, 0.2 mm width, and 0.2 mm spacing between them on PCBs. The PCB is detailed in Figure S1 of the Supporting Information file (SI).

For film deposition, a mixture of high-purity Ar (99.999%) and N_2 (99.999%) is introduced into the reactor chamber. The Ar:N_2 ratio is a critical parameter for nitride formation. The deposition pressure is kept at ∼1 Pa with a downstream throttle automatic control system, and the RF power is kept at 150 W throughout the process. The first two types of films (HEN-1 and HEN-2) differed in the Ar:N_2 ratio during deposition, with ratios of 10:1 (10 sccm of Ar and 1 sccm of N_2) and 1:10 (1 sccm of Ar and 10 sccm of N_2), respectively. Both types of films are deposited with substrates parked parallel to the target surface (0°). The third film (HEN-3) maintains the 1:10 ratio but is deposited at an 85° angle relative to the target (glancing angle geometry). All films are deposited without external or intentional substrate heating for 90 min. Although the substrate temperature increased to ∼55 °C during sputtering due to the plasma effect, the temperature is stabilized after a time of <5% of the total deposition step. The first set of samples on Si is used to determine the growth rate, which is applied in subsequent depositions. The thickness of the HEN films on the PCBs is ∼150 nm.

2.2. Film Characterization. The microstructure and thickness of the films are assessed through cross-sectional analysis by field-emission-gun scanning electron microscopy (FEG-SEM, Zeiss Supra 40). The crystallographic structure is obtained via X-ray diffraction (XRD, Shimadzu XRD-6000) in the Bragg−Brentano (θ−2θ) configuration, equipped with a monochromatic Cu Kα (λ = 1.54056 Å) radiation source. The measurements were conducted with a step size of 0.05° and a scan rate of 0.5°/min. Micro Raman spectroscopy at room temperature is performed in a backscattering configuration with a 632.8 nm excitation source (RM2000 - Renishaw) for samples on Si substrates. Similar measurements on PCB gold digits are carried out under similar conditions using XploRA equipment (Horiba) with a 638 nm excitation source. These measurements were specifically employed to assess the structural durability of the HEN films after repeated usage. Approximately 200 measurement cycles, involving sequential exposure to solutions and flushing steps, were performed on the e-tongue device.

X-ray photoelectron spectroscopy (XPS) is employed to determine the relative films' atomic composition and chemical states with 1486.6 eV photons (no monochromatized) from an Al target (Kα line) using a Thermo Alpha 110 hemispherical analyzer in Constant Energy Mode (CEM) and pass energy of 20 eV. An *in situ* cleaned silver standard sample is used to calibrate the binding energy scale of the instrument, referencing the $3d^{5/2}$ electrons at 368.2 ± 0.1 eV. The silver sample is also employed to determine the analyzer's work function.

Survey and individual elements' XPS spectra are recorded *ex situ*. The cleaning is conducted in an ion-beam-assisted deposition (IBAD) system coupled to the XPS chamber. The Ar^+ ions generated by a 1-in. diameter Kaufman cell sputtered the surface for 2 min with 400 eV energy and a nominal current of ∼20 mA (current density of ∼0.18 mA/cm^2).[52] The experimental XPS spectra are processed using ThermoAdvantage and CasaXPS[53] software, and the Shirley method is employed to remove the inelastic electron scattering background. Gaussian−Lorentzian mix functions are employed to fit experimental data and identify spectral bands.[54]

2.3. Microfluidic e-Tongue Impedance Measurements. The microfluidic e-tongue device setup layout, developed and optimized previously in our group,[55−57] comprises four colinear IDES printed on a PCB (multisensor gadget), a microchannel, and the measurement apparatus, as shown in Figure S2. The microchannel is fabricated with polydimethylsiloxane (PDMS) molding, having approximately 500 μm width and height and 4 cm length. Detailed descriptions of the microfluidic device are available in previously published work.[57,58]

Impedance measurements are performed with an input signal having 25 ± 1 mV AC voltage amplitude across a frequency range of 1−10^6 Hz with a Solartron 1260A phase gain/impedance analyzer. The study solution is injected into the microchannel at a constant flow rate (15 mL/h) by a syringe pump, ensuring exposure (quasi-equilibrium) of the solution to the active surface of the thin film HEN of the e-tongue device. The flow rate was previously optimized by adjusting the sample volume flowing continuously, a more efficient method when compared to static measurements.[58]

Five independent measurements are taken from each sample, and after each test, the microchannel is cleansed by flushing ∼5 mL of ultrapure water (18 MΩ) to prevent cross-contamination. Two protocols are determined to verify sensor performance. The first consists of using 1 mmol/L aqueous KCl and NaCl solutions and pure water. Potassium and sodium ions (K+ and Na+, respectively) are purposefully chosen to check the sensor resolution response, as they are very similar in size and properties. The second test uses electrolytes and nonelectrolyte solutions mimicking basic taste profiles.[56] Briefly, 1 mmol/L aqueous solutions were prepared of sucrose (sweetness), NaCl (saltness), HCl (sourness), caffeine (bitterness), and L-glutamic acid (umami). With that, we can test both the sensor response to electrolyte and nonelectrolyte solutions and the distinction of different compounds separately identified on the human palate.

As remarked in the Introduction, statistical methods are applied to identify sample fingerprints, correlations, and patterns due to the large volume of data generated during measurements. First, Principal Component Analysis (PCA) is employed for exploratory analysis and pattern recognition.[59] Briefly, it compresses data into smaller dimensions while preserving relationships between the attributes of the samples. The so-called *first principal component* (PC1) captures the largest variance, and the *second principal component* (PC2) captures the next largest variance and is orthogonal to PC1 to minimize information redundancy, and so on. The axes (1, 2, etc.) are

https://doi.org/10.1021/acsaelm.5c00489
ACS Appl. Electron. Mater. 2025, 7, 5537−5548

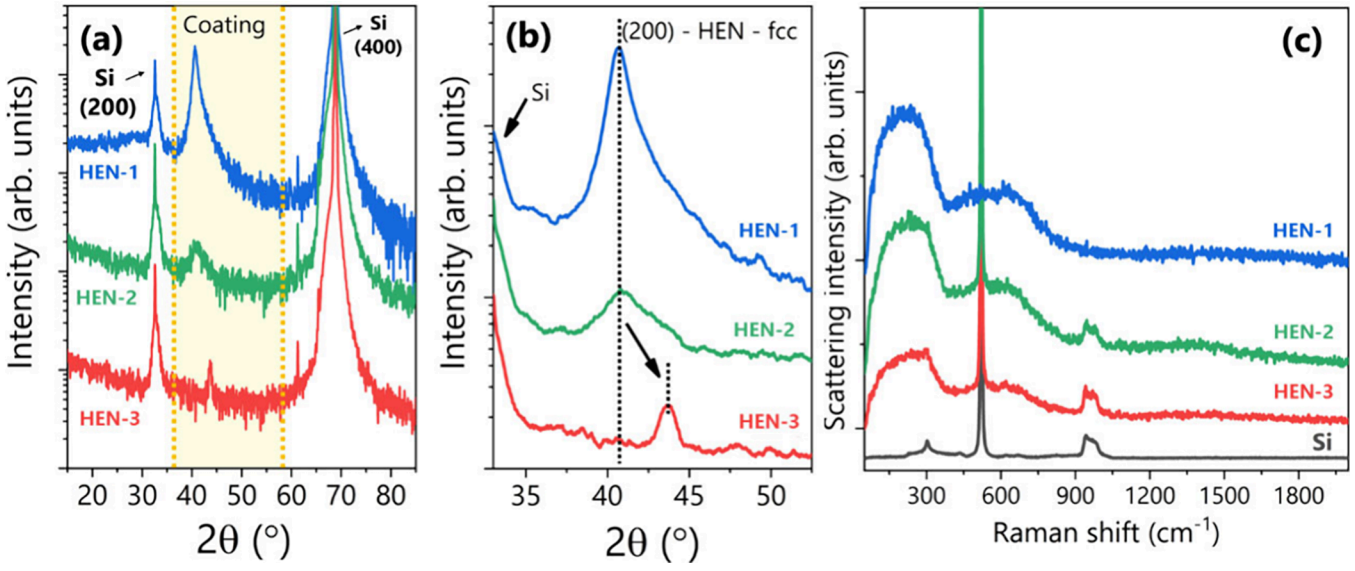

Figure 2. In (a) and (b), respectively, the full range X-ray diffractogram and the zoomed subplot for the film region are presented for the three films. (c) Raman spectra for the same films are displayed.

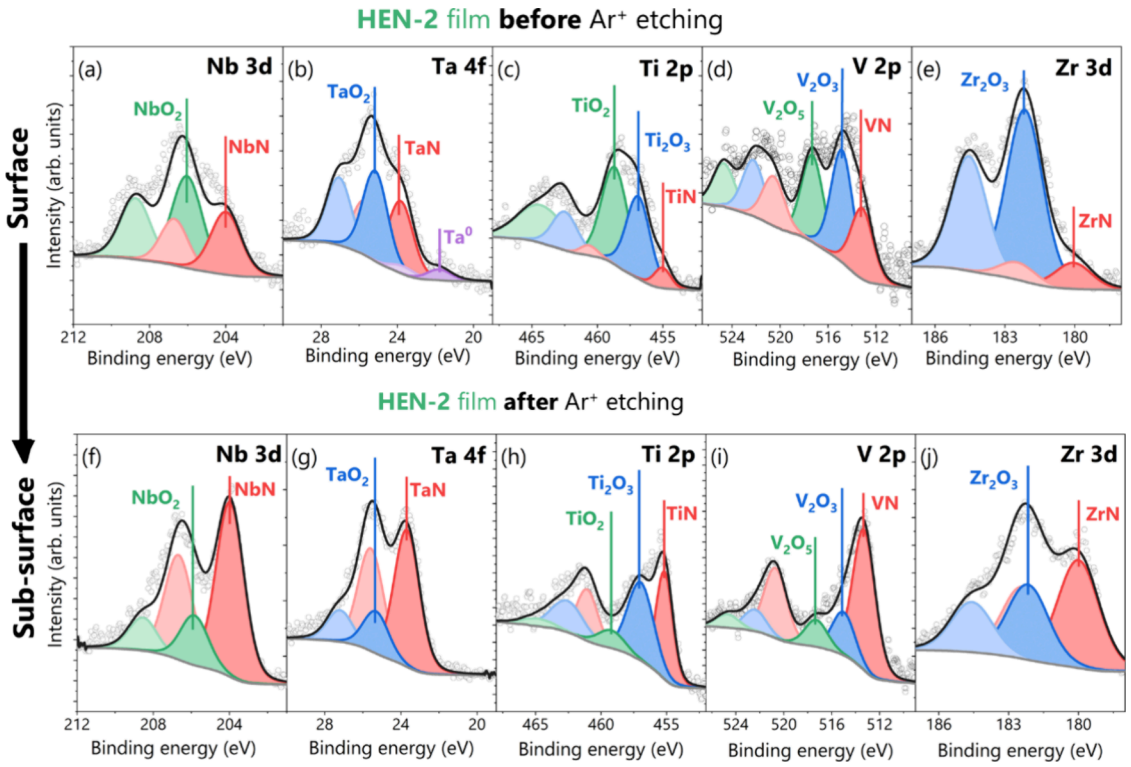

Figure 3. Details of the *ex situ* XPS spectra measurements corresponding to the five transition metals (Nb, Ta, Ti, V, and Zr) of the HEN-2 coating's surface sensor presented from (a) to (e) before cleaning and etching. Additionally, the chemical environments for the same elements are shown after *in situ* argon etching, from (f) to (j) as reported in the Film Characterization section.

orthogonal, ensuring unique information on each PC. The number of PCs is determined by analyzing the variance explained by each component and the cumulative variance percentage. Raw data is normalized and mean-centered before PCA analysis.[60]

3. RESULTS AND DISCUSSION

Before the device assembly, HEN film characterization is carried out carefully. The deposition technique described above (Materials and Methods) of the high entropy films is similar to that used in previous work,[51,52] as illustrated in Figure 1(a). To determine the deposition rate for each of the three conditions of film deposition, deposits of identical growth parameters and time are carried out on Si (100) wafers.

3.1. Scanning Electron Microscopy (SEM), X-ray Diffraction Analysis, and Raman Spectroscopy. *3.1.1. Scanning Electron Microscopy (SEM).* Figure 1(b), (c), and (d) shows cross-sectional micrographs for the three films. A columnar structure is observed in all cases. It is important to note that the depositions are performed without intentional substrate heating, and the maximum substrate

https://doi.org/10.1021/acsaelm.5c00489
ACS Appl. Electron. Mater. 2025, 7, 5537−5548

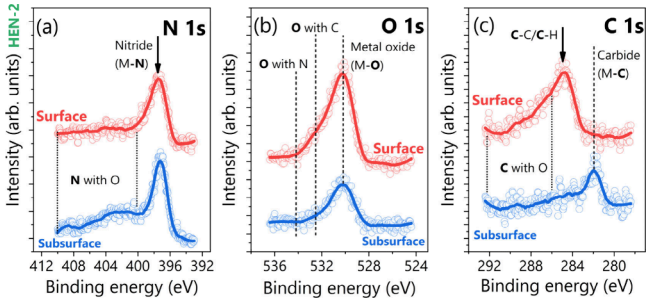

Figure 4. Transition of (a) N, (b) O, and (c) C signals before (surface) and after (subsurface) argon etching of the surface of the HEN-2 film.

temperature during deposition, due to plasma heating, was approximately 55 °C. In our deposition system, all plasma process parameters (pressure, plasma power, target−substrate distance) are kept constant. In previous works conducted under these exact same conditions but without nitrogen addition, the resulting films exhibited an amorphous metallic glass structure.[51] The only modification in the current process is the introduction of nitrogen into the sputtering atmosphere. This change led to the formation of crystalline structures even at low substrate temperatures. However, stress and bombardment cannot be ruled out as contributing factors to the crystallization of the alloys. Therefore, we attribute the observed crystallization primarily to the nitrogen incorporation, which promotes nitride formation and structural ordering among the metal species in the high-entropy alloy. This behavior is crucial for the intended application, as it enables low-temperature processing (<100 °C) while ensuring the mechanical and chemical stability of the sensing units.

The nitrogen content during film growth significantly influences the deposition rate compared with pure metal high-entropy alloys. For HEN-1, deposited with the lowest N_2 proportion, the sputtering process operates predominantly in the metal mode, characterized by high sputter yields and consequently higher deposition rates, resulting in films approximately ten times thicker. As the nitrogen concentration increases (as in HEN-2 and HEN-3), the system transitions into the poison mode, where the formation of nitrides on the target surface reduces the sputtering yield, leading to lower deposition rates.[62,63] Between the HEN-2 and HEN-3 films, which were grown under the same gas composition but with varying substrate angles (0° to 85°), no significant microstructural differences are observed in the current micrographs, and only slight thickness variations within the experimental uncertainty are noted, as shown in Figures 1(c) and 1(d).

3.1.2. X-ray Diffraction Analysis. Figure 2(a) and (b) shows the XRD diffractograms in full range and a detailed view of the film-related region, respectively. Initially, the expected contributions from the Si substrate can be identified due to the thin film thickness being in the nanometric range. Moreover, the peak at around 61.5° 2θ corresponds to the Cu $K\beta$ contribution. These well-defined peaks assist in aligning the measurements, allowing a better discussion of the variations observed between 35° and 50°, where the film's structure is evident. The peak around 40° is already reported and attributed to the reflection associated with the (200) plane of the face-centered cubic (*fcc*) structure of high-entropy nitride (HEN) films.[36] Such a structure suggests that the coating is a solid solution phase, instead of a mix of regions with binary nitrides, and that N may be present in the coating as interstitial atoms.[64] The stability of this single phase is a direct consequence of the high entropy effect, which significantly reduces the free energy of the solution phase compared to that of the simple binary nitrides.[65]

Comparing the first two films, it is observed that the peak positions are similar, but the peak broadens with a higher nitrogen content during deposition. Indeed, nitrogen saturation may lead to defects, distortions, or structural modifications.[62] The target poisoning effect and differential sputtering yield could hinder significant grain growth. The positive peak shift associated with (200) reflection has been associated with a lattice contraction effect (Figure 2(b)).[49,66] Changing the deposition angle modifies the precursors' impinging angle and energy of the arriving species, affecting the microstructure of the growing film. In our case, deposition at high angles likely reduces the surface diffusion and promotes the growth of more isolated columnar structures, where local stresses may accumulate more significantly. This stress accumulation leads to a compressive strain in the lattice, resulting in a slight contraction of the interplanar spacing. According to Bragg's law, this contraction shifts the diffraction peaks (such as the 200 reflection) toward higher 2θ angles, as observed experimentally. However, given the possible nanocrystalline nature of the films, the broadness and slight asymmetry may be attributed primarily to grain size distribution and microstrain, i.e., inhomogeneous broadening and local stress. Additionally, minor changes in chemical composition (e.g., oxygen and nitrogen incorporation) could also contribute to the stress state and slight lattice parameter variations. In agreement with previous works, the substrate

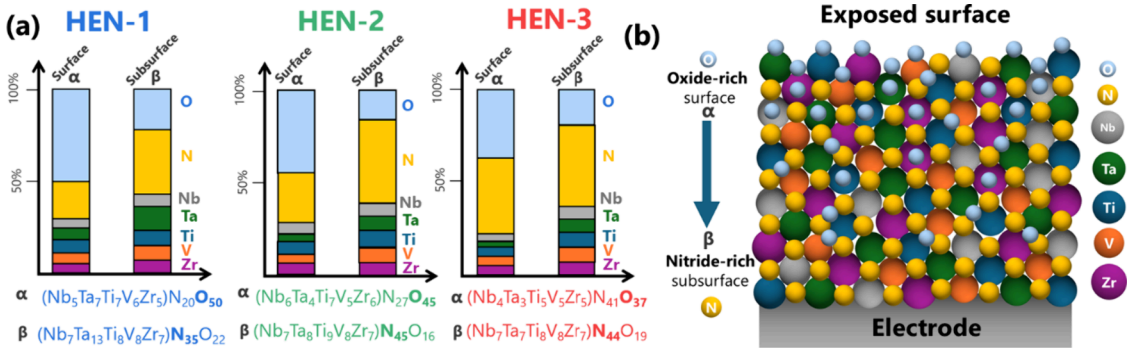

Figure 5. (a) Schematic of the films' composition and (b) atomic structure along with the atomic composition of each film deposited, for both the surface and subsurface, obtained by XPS.

https://doi.org/10.1021/acsaelm.5c00489
ACS Appl. Electron. Mater. 2025, 7, 5537−5548

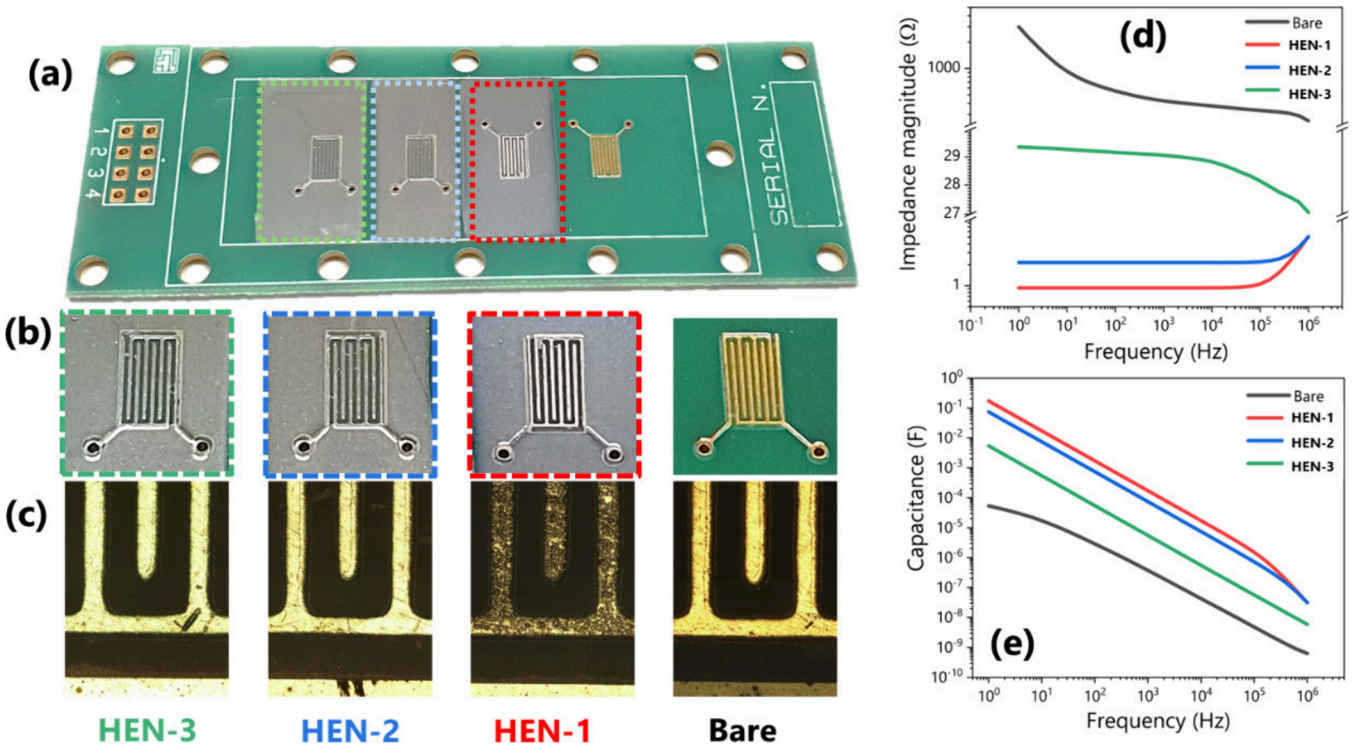

Figure 6. (a) Resulting HEN-based e-tongue device, (b) detailed images, (c) optical picture micrographs of the electrodes, and (d, e) the impedance and associated capacitance magnitude measured on each sensing unit in contact with ultrapure water (benchmark), showing that the electrical responses are different on each IDE.

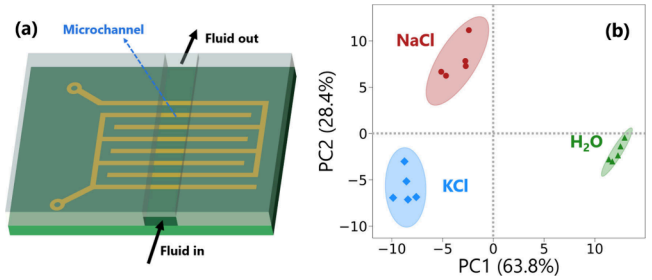

Figure 7. (a) Schematic illustration of a single interdigitated electrode (IDE) integrated with a microchannel to perform electrical measurements. The complete e-tongue assembly consists of a "sandwich" structure formed by the bottom printed circuit board (green), the IDE array (golden), and a top transparent polymer layer (gray) containing the sculpted microchannel (dark green) through which the fluid flows. The e-tongue device is composed of four IDEs (three coated with distinct HEN films and one bare; please see Figure 6 (a)), whose combined responses form the sensor output. (b) Principal component analysis (PCA) plot of five independent measurements for three different liquid media: distilled water, NaCl, and KCl solutions. The ellipses represent 95% confidence intervals for each cluster.

motion during deposition, with all other parameters held constant, by itself, modifies the micro- and nanostructure.[48]

It is well established that transition metal nitrides with FCC structure tend to grow (111)-oriented under low ion-to-neutral flux conditions. At the same time, the (200) orientation is favored under higher energy bombardment, typically achieved via substrate biasing or high ionization plasmas. One may note that in this set of samples the (200) orientation is predominant.

It is important to highlight that thickness plays a critical role in the texture evolution of *fcc* nitrides. As described in the literature,[67] transition metal nitrides in general initially grow with strong (200) texture in thin films, and only for thicknesses above ∼200−300 nm does a gradual transition toward (111) preferred orientation become noticeable. Moreover, a similar effect is also visible in other systems with high-entropy nitride coatings (such as *AlCrNbSiTiVN*, *AlCrNbSiTaTiVN*, and *AlCrNbSiTaTiVZr*) of a thickness of ∼1 μm.[68] Considering the floating potential and the thickness of the coatings, the growing film is subjected to (Ar^+, N_2^+) ion bombardment due to the self-bias floating potential, which can explain the preferential growth of the (200) orientation in the current setup.

3.1.3. Micro Raman Spectroscopy. Figure 2(c) shows the Raman spectra for all sensing units and a reference substrate. Overall, all three active films exhibit similar features consisting of two main bands. A recent study by Pshyk et al.[69] suggests that for films similar to those studied here, but with varying levels of Al addition, the Raman shift in HENs is preferentially determined by symmetry breaking due to a severely distorted cation sublattice caused by atomic size mismatch between the metal elements. Additionally, transition metal nitrides are scattered due to deviation from stoichiometry and the associated formation of vacancies or antisite defects. The Raman spectra presented here agree with those in the cited work,[69] where the films show first-order transverse and longitudinal bands in the acoustic frequency range and first-order optical modes in the optical frequency range.

3.2. Chemical Composition and Structure of the Films. XPS is employed to evaluate the chemical properties of the films, analyzing both the surface (analysis depth of ∼5 nm[54]) and underneath after removing surface contamination by argon sputtering (see Film Characterization section). As the impedance of the sensing units is strongly dependent on both

https://doi.org/10.1021/acsaelm.5c00489
ACS Appl. Electron. Mater. 2025, 7, 5537−5548

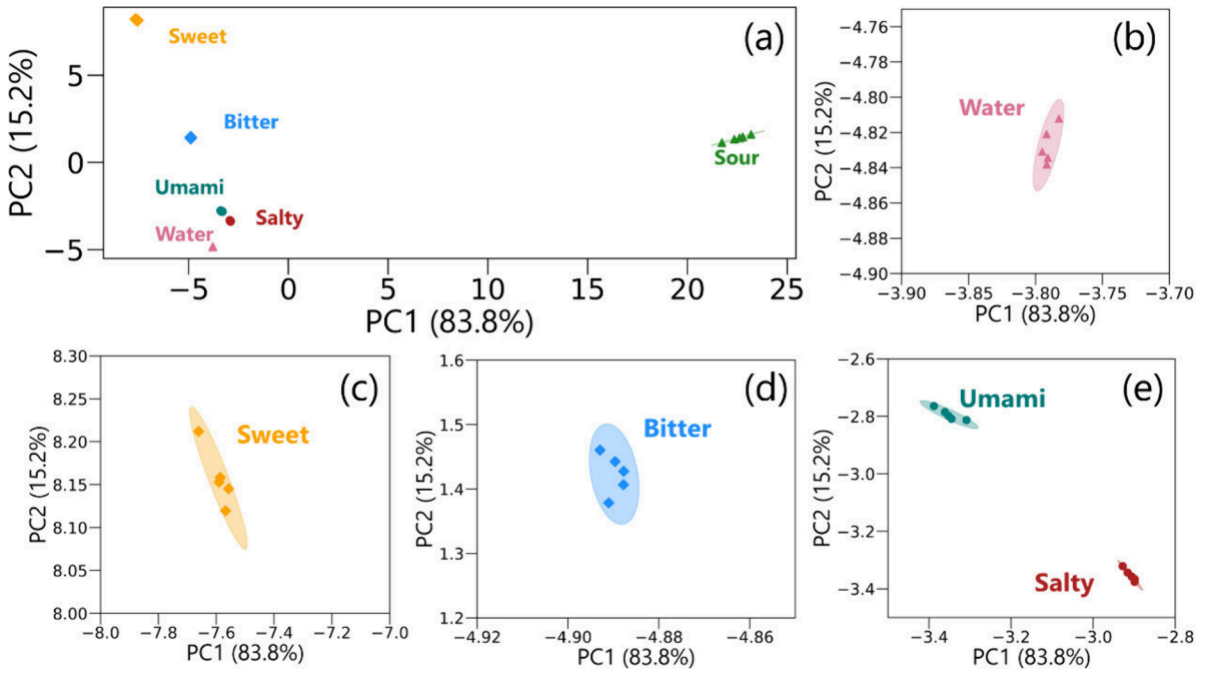

Figure 8. (a) PCA plot for the test with solution mimicking the five basic tastes for human gustatory perception at a concentration of 1 mmol/L. From (b) to (e), zoomed areas for the different regions of the plot are shown, helping to identify the ellipses that represent a confidence level of 95%.

the HEN film's dielectric characteristics and the electrode's geometric properties, control of these properties provides valuable insights related to the electric device response. The deconvolution of the individual contributions is carried out for all the samples studied (see Supporting Information). As an example, the results from XPS are presented for the sample HEN-2 film as shown in Figure 3, with peak attribution following previous results compiled in the references.[51,70,71] Figure 3(a)−(e) shows the predominant presence of M−O oxidized and the M−N bonds, where M means the transition metal. The expected doublet-shaped contributions due to the electrons of the 2p level to the spin−orbit interaction for the transition metals are present.[54] It is remarked that only Ta, in Figure 3(b), shows a metallic contribution (Ta°). The presence of pure metal species, even after surface environmental exposure, has been reported previously.[61] The same response for the other two films is shown in Figures S3 and S4. Confirming the previously suggested incomplete nitridation of the HEN-1 film, it is observed that Ti and Zr also show metallic contributions, which are not observed in the other two films. As reported later, this bonding structure is also present deeper into the film. The formation of metallic oxides during deposition is due to ubiquitous residual oxygen in the deposition chamber and is also caused by surface oxidation from postdeposition exposure to the ambient atmosphere.[51]

The film characterization section also details eroded samples by employing the ion beam to draw information about the bulk region of the film. After the process, the sample is transferred to the XPS system through an ultrahigh vacuum chamber, minimizing the possibility of contamination and oxidation. The most significant change is the increase in the contribution of M−N bonds, while M−O bonds become less intense. Since the deposition process is carried out under very low base pressure, the presence of oxygen is reduced but never eliminated. In the case of samples deposited in a nitrogen-rich atmosphere, no indications of purely metallic contributions are present in this region. On the other hand, the sample with lower N_2 content during deposition still shows the presence of Zr° and Ti° in the structure.

Figure 4 shows the bands associated with electrons for the (a) N 1s, (b) O 1s, and (c) C 1s levels of the HEN-2 sample, confirming these observations. Initially, the chemical environment for nitrogen indicates an increase in the intensity of the contribution related to the presence of nitrides at the surface. Additionally, during etching, oxygen from the material may be incorporated into the nitrogenated structure due to the energy expended in the process (although the contribution is marginal). It is important to emphasize that the HEN-1 sample exhibits a very weak peak for M−N bonding at the surface, which is much more evident in the subsurface. The relatively largest contribution, as denoted in Figure 4(b), is related to metallic oxides. This component is located within the expected range for transition metal oxides. The much stronger M−O peak may mask other components such as N−O and C−O. A hint of this behavior was already seen in the previous data, where the lower nitrogen content allowed for greater surface oxidation when exposed. The behavior of oxygen is similar for all three samples. Figures S5 and S6 (Supporting Information) present the same analysis for the other two samples in the series.

Regarding the band associated with electrons in C 1s orbitals, Figure 4(c) shows a typical behavior for this analysis: on the surface, a high carbon content is always present in samples exposed to the ambient atmosphere before ion beam etching. This element originates from the well-known adventitious carbon, which in this case can be observed at an energy of ∼284.8 eV. Part of it also comes from the absorption of oxygenated carbon species, such as CO_2. Once the topmost layer is removed by argon sputtering, the carbon contribution becomes marginal, drastically reducing the peak. A small contribution to lower energies, indicating the presence of carbides, can be observed, too. We infer that such a bond may

https://doi.org/10.1021/acsaelm.5c00489
ACS Appl. Electron. Mater. 2025, 7, 5537−5548

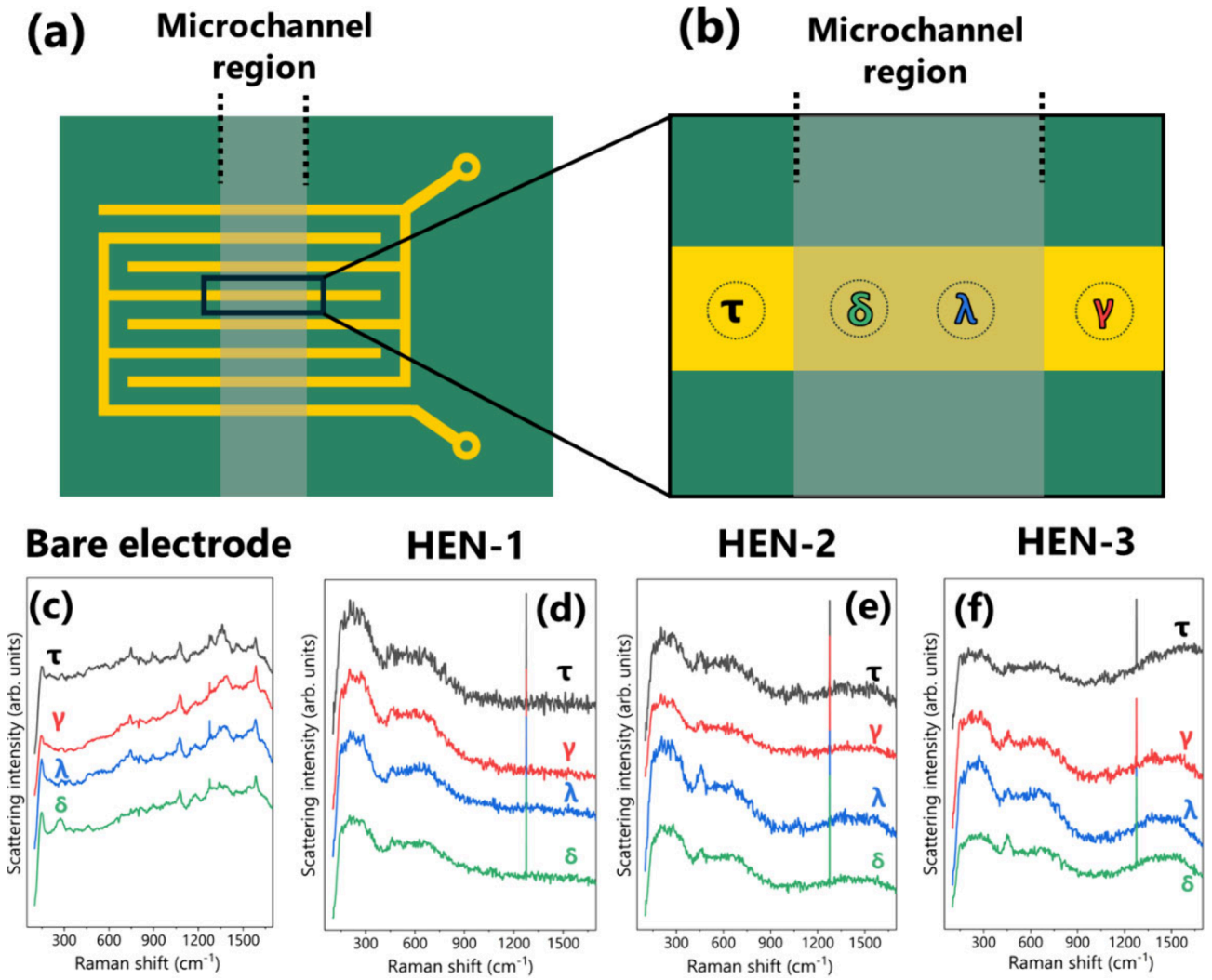

Figure 9. Robustness test for the sensor array after approximately 200 measurements and flushing cycles. (a,b) Schematic representations of the IDEs. The dashed lines indicate the microchannel region exposed to fluid flow during the tests. τ and δ denote regions not submitted to liquid flow, while γ and λ correspond to regions inside the microchannel. Raman spectra acquired from these regions after the durability tests are shown from (c) to (f), respectively.

arise from sputtering mixing during the etching and cleaning process.[72] The same behavior is observed for the other two films in Figures S5 and S6 of the SI. Considering the intended application, it is important to note that the outermost interface is constantly exposed to fluids when the sensor is in operation. Since oxide is a robust surface for the environment, this surface passivation may aid in the stability of the sensor signal.

3.3. In-Depth Chemical Composition of the Studied HEN Films. From the information gathered in the last section, a graphical composition distribution of the samples is shown in Figure 5(a) for the two regions denoted from now on as α and β, respectively. The relative atomic composition is also shown.

For all three samples studied, the following observations are highlighted: a) they all exhibit relatively higher oxygen content at the surface, which decreases in depth while nitrogen content increases, and b) the ratio of metallic elements is near-equimolar in all deposition conditions, with the largest deviation observed in the first condition, where lower nitrogen content was used during deposition. It is worth noting that, for all samples, the carbon contribution is ∼22 at. % at the surface and ∼7 at. % underneath. Carbon is disregarded for determining the chemical formulas. It mainly originates from adventitious carbon and is expected to be contaminated during deposition/etching; therefore, it will be discussed later. Surface oxidation is expected for all samples exposed to ambient air. We remark that there is a lower oxygen concentration for samples deposited with a higher nitrogen content as the passivation of the metallic atoms by nitrogen is already in place. Even in the subsurface, the nitrogen concentration is lower for the first sample, suggesting that metal nitridation is incomplete, leaving room for purely metallic and/or oxidized contributions from these elements. Finally, a schematic representation of the material is presented in Figure 5(b), showing the transition from an oxide-rich interface to a nitride-rich interface, i.e., the latter forming a crystalline solid solution since the material components are near equimolar.

The presence of a thin oxide-rich surface layer atop the HEN films, combined with a conductive nitride subsurface, is expected to influence the impedance spectra by introducing additional interfacial resistance and capacitance contributions, particularly at low frequencies. This layered structure enhances the chemical stability while preserving sufficient electronic conduction pathways through the underlying nitride phase. Such surface−subsurface interactions are characteristic of

https://doi.org/10.1021/acsaelm.5c00489
ACS Appl. Electron. Mater. 2025, 7, 5537−5548

layered structures and can play a significant role in tuning both the sensitivity and durability of impedance-based sensing devices.

3.4. Electrical Characterization. Once comprehensively characterized by the deposition parameters, the films are grown onto IDEs collinearly placed on a printed circuit board (PCB). Each PCB has four IDEs, one left bare to serve as a control and comparison (bare unit). It is worth highlighting that thin film deposition by plasma techniques in e-tongues is innovative and has recently been developed in our group. Figure 6(a) shows a photograph of the complete PCB, and in Figure 6(b), a detail of each electrode is shown. At first glance, a drastic color change and efficient deposition are suggested on both the electrode and the polymer. Optical microscopy micrographs are shown in Figure 6(c) for distinct electrode regions. Despite plasma treatment, no degradation is observed in any component of the IDEs. The physical integrity of the electrode is maintained, while the nanometric film is deposited. As mentioned earlier, one of the conditions for forming an electronic tongue is sensing units exhibiting distinct electrical responses under the same conditions (e.g., different excitation signal when in contact with the same fluid). Film characterization showed that they have different structures, but assessing whether these modifications are sufficient to alter the electrical response is necessary. The four electrodes are electrically tested in contact with ultrapure water to do so.

Figure 6(d) presents the impedance magnitude (in ohms) as a function of frequency (in Hz). Figure 6(e) shows capacitance data for the exact measurements, a property that can also be used in comparative tests using equivalent electric circuits. Compared to the bare electrode, one can conclude that the HEN films on the IDEs substantially modify the electrical response qualitatively and quantitatively. The HEN-1 and HEN-2 films present similar curves with low impedance values. This behavior indicates a resistive behavior for more conductive films, due to either the electrical properties of the film itself or the material's nanostructure, as depicted by SEM and X-ray diffraction data. Although seemingly simple, these results show that we can fine tune high-entropy nitrides for the e-tongue case.

Two tests were designed as proofs-of-concept for the HEN-based electronic tongue. The first test evaluates the ability of the e-tongue to differentiate similar aqueous solutions at identical molar concentrations (1 mmol/L), while the second assesses its capability to distinguish the basic tastes perceived by the human tongue at concentrations close to or below the human detection threshold.[56]

Figure 7(a) schematically illustrates a single interdigitated electrode (IDE) integrated into the microfluidic channel through which the analyte flows during measurement. The complete e-tongue device consists of an array of four IDEs (three HEN-coated and one bare), whose combined electrical responses are used to generate characteristic fingerprints for each solution, as further analyzed by PCA.

Figure 7(b) is the PCA score plot for five independent measurements of each fluid in each sensing unit. The ellipses drawn around the data points are generated from the Mahalanobis distance (MD)[73] with a 95% confidence level. Briefly, Mahalanobis distance is a powerful tool for comprehending the structure of multivariate data and their interrelationships. It is a measure that considers the correlation among the variables in a data set. It is especially useful in contexts where the variables have different scales or are correlated. Overall, these ellipses illustrate clusters of measurements that have similar fingerprints. Summing up: ellipses with overlapping or joining measurements of distinct samples may indicate poor device performance and *vice versa*. Moreover, with a silhouette coefficient of 0.848, it is possible to conclude, with great confidence, that the classification of the data set ensures high resolution of the data displayed in Figure 7.[74] Water is located in the region of positive PC1 values, while saline solutions are in the negative area, indicating good discrimination since this axis may differentiate salt concentration. The PC2 axis helps to separate the two ions: Na^+ for PC2 > 0 and K^+ for PC2 < 0, with pure water positioned at the (10, 0) coordinate. Therefore, the variation in the electrical response of the electrodes and its statistical analysis by PCA confirms the efficient performance of the device in separating these patterns, even considering samples with very similar tastes. It is important to note that the two PCs, PC1 and PC2, are sufficient to describe 92.2% of the data variance (PC1 + PC2, as reported in the axis of Figure 7(b)).

Figure 8(a) shows the PCA score plot for the second test, presenting a more complex scenario with samples having distinct properties. For clarity, Figure 8(b)−(e) shows zoomed-in sections of different areas from Figure 8 for the analysis of fundamental taste patterns. It is worth mentioning that the concentrations of sweetness, saltiness, and umami are close to or below the human threshold perception.[75] The overall plot resolves the six samples tested. It is essential to notice that each region results from five independent measurements. Notably, the cluster corresponding to the sour taste (HCl solution) exhibits the most significant displacement in the PCA due to the high ionic mobility in this sort of solution since the mobility of the H^+ ion exceeds the mobility of the Na^+ and Cl^-. The separation is so efficient that overall the points from the independent measurements overlap, and the confidence ellipse is not visible. The subplot series confirms the points' low dispersion and graphically illustrates an *archipelago* well resolved of different tastes. The calculated silhouette coefficient of 0.974 confirms the robustness of the classification in agreement with standards accepted in the literature.[74] Moreover, the sum of PC1 and PC2 describes 99% of the total variance in the data.

The positive results from the two tests confirm the efficiency of employing high-entropy nitride-coated sensing units in a microfluidic impedimetric e-tongue system. Raman spectroscopy corroborates the integrity of the active HEN coating after the aging test. In total, the number of measurements may reach ∼200, including the evaluation of solution with similar ions and the distinct flavors, as well as the repeated flushing after each analyte. Figure 9 presents the Raman spectra obtained in different zones of the HEN coating, as indicated in Figure 9(a). The Raman spectra of the zones where the liquid flows (δ, λ) and the areas that are not in contact with the fluid (τ, γ) are compared. The spectra from exposed and nonexposed regions show no significant spectral shifts, peak broadening, or intensity loss, indicating that fluid exposure did not induce detectable chemical or structural changes in the HEN films. The results show that the Raman scattering pattern is similar for each of the four electrodes. The Raman spectra of the films are very close to those presented in Figure 2(c), with all films keeping the same structure and their chemical and physical integrities. This direct comparison further confirms the chemical robustness of the coatings, even under repeated fluid flow conditions.

https://doi.org/10.1021/acsaelm.5c00489
ACS Appl. Electron. Mater. 2025, 7, 5537−5548

It indicates that even after several uses they still protect the electrodes, preserving distinct electrical responses that allow the sample identification. It is important to emphasize that these tests represent an initial assessment of the system's robustness. Extended durability tests, involving a larger number of measurement cycles, should be performed to further evaluate the long-term stability of the coatings and their protective function.

4. CONCLUSION

This study presents a novel e-tongue utilizing high-entropy nitride (HEN) films, where five transition metals (Nb, Ta, Ti, V, and Zr) form an *fcc* nitride solid solution, deposited by RF sputtering. The near-equimolar incorporation of multiple metals enhances the material's properties compared to their individual binary nitrides, including a more active surface for interaction with different analytes. High-entropy nitrides provide exceptional chemical and structural stability, tunable electrical properties, and strong resistance to degradation, making them excellent candidates for enhancing sensor performance. The precise control over microstructural and electrical properties of HEN films, achieved through optimized deposition parameters, directly enhances the sensor performance.

When these coatings are grown on interdigitated electrodes, they produce distinct electrical responses to aqueous systems flowing through a microchannel, enabling the formation of unique electrical fingerprints for sample identification. Additionally, optimized deposition at low substrate temperatures preserves the integrity of the films on IDEs collinearly placed on printed circuit boards. The impedimetric e-tongue response enables an accurate analysis of all tested samples. A robust statistical analysis, including principal component analysis (PCA) and silhouette coefficient methods, confirms the device's ability to reliably distinguish between K^+ and Na^+ ions and different tastes, demonstrating high resolution and reproducibility. Furthermore, the sensor maintains excellent physical and chemical stability after extensive testing (~200 measurements), indicating long-term functionality. These findings position HEN-based sensors as a promising platform for real-world applications including but not limited to environmental monitoring and food analysis.

■ ASSOCIATED CONTENT

Supporting Information

The Supporting Information is available free of charge at https://pubs.acs.org/doi/10.1021/acsaelm.5c00489.

Additional details of the project, floating potential calculation, XPS spectra table – Table S1; detailed scheme of the printed circuit board (PCB) and interdigitated electrodes (IDEs) – Figure S1; measurement setup for the e-tongue device – Figure S2; individual XPS spectra of the five transition metals forming HEN-1 and HEN-3 films before and after argon ion etching – Figure S3 and S4; individual XPS spectra of nitrogen, oxygen, and carbon for the HEN-1 and HEN-3 films before and after argon ion etching – Figures S5 and S6 (PDF)

■ AUTHOR INFORMATION

Corresponding Authors

Leonardo M. Leidens – *Instituto de Física 'Gleb Wataghin' (IFGW), Universidade Estadual de Campinas (UNICAMP), 13083-970 Campinas, SP, Brazil;* orcid.org/0000-0003-4552-1013; Email: leidens@unicamp.br

Antonio Riul, Jr. – *Instituto de Física 'Gleb Wataghin' (IFGW), Universidade Estadual de Campinas (UNICAMP), 13083-970 Campinas, SP, Brazil;* orcid.org/0000-0002-9760-1851; Email: riul@unicamp.br

Authors

Carla D. Boeira – *Instituto de Física 'Gleb Wataghin' (IFGW), Universidade Estadual de Campinas (UNICAMP), 13083-970 Campinas, SP, Brazil*

Maria H. Gonçalves – *Instituto de Física 'Gleb Wataghin' (IFGW), Universidade Estadual de Campinas (UNICAMP), 13083-970 Campinas, SP, Brazil*

Endel E. C. Costa – *Instituto de Física 'Gleb Wataghin' (IFGW), Universidade Estadual de Campinas (UNICAMP), 13083-970 Campinas, SP, Brazil*

María C. Marchi – *Universidad de Buenos Aires, Facultad de Ciencias Exactas y Naturales, Departamento de Química Inorgánica, Analítica y Química Física, C1428EGA Buenos Aires, Argentina; CONICET - Universidad de Buenos Aires, Instituto de Física de Buenos Aires (IFIBA), Centro de Microscopías Avanzadas (CMA), C1428EHA Buenos Aires, Argentina*

Antonio R. Zanatta – *Instituto de Física de São Carlos (IFSC), Universidade de São Paulo (USP), 13560-970 São Carlos, SP, Brazil*

Fernando Alvarez – *Instituto de Física 'Gleb Wataghin' (IFGW), Universidade Estadual de Campinas (UNICAMP), 13083-970 Campinas, SP, Brazil;* orcid.org/0000-0002-9393-1298

Complete contact information is available at: https://pubs.acs.org/10.1021/acsaelm.5c00489

Funding

The Article Processing Charge for the publication of this research was funded by the Coordenacao de Aperfeicoamento de Pessoal de Nivel Superior (CAPES), Brazil (ROR identifier: 00x0ma614).

Notes

The authors declare no competing financial interest.

■ ACKNOWLEDGMENTS

This study was financed, in part, by the Fundação de Amparo à Pesquisa do Estado de São Paulo (FAPESP), Fundação de Amparo à Pesquisa do Estado do Rio Grande do Sul (FAPERGS) – Project 2019/18460-4 – FAPESP-FAPERGS, INCT-INES (CNPq #465423/2014-0), CNPq #403359/2023-6, CNPq #308943/2021-0, Brazil. C.D.B (grant #2022/08216-1) and L.M.L. (grant# 2023/07552-0) are FAPESP Fellows. M.C.M. acknowledges project PICT-2021-GRF-TI-00303. F.A., A. R. Z, and A.R. Jr. are CNPq Fellows. The authors are grateful for the support and infrastructure of LAMULT-IFGW.

REFERENCES

(1) Shimizu, F. M.; Braunger, M. L.; Riul, A. *Electronic Tongues*; Shimizu, F. M., Braunger, M. L., Riul, A., Eds.; IOP Publishing, 2021. DOI: 10.1088/978-0-7503-3687-1.

(2) Vlasov, Y.; Legin, A.; Rudnitskaya, A.; Di Natale, C.; D'Amico, A. Nonspecific Sensor Arrays ("electronic Tongue") for Chemical Analysis of Liquids: (IUPAC Technical Report). *Pure Appl. Chem.* **2005**, *77* (11), 1965−1983.

(3) Pereira, T. S.; Facure, M. H. M.; Mercante, L. A.; Gonçalves de Souza, M. H.; Braunger, M. L.; Riul, A., Jr; Correa, D. S. Electronic Tongues: Basics, Materials, and Applications. *Nature-Inspired Sensors* **2025**, 451−465.

(4) del Valle, M. Sensor Arrays and Electronic Tongue Systems. *Int. J. Electrochem.* **2012**, *2012*, 1−11.

(5) Tahara, Y.; Toko, K. Electronic Tongues-a Review. *IEEE Sens. J.* **2013**, *13* (8), 3001−3011.

(6) Kossakowska, A.; Kociszewska, K.; Kochman, K.; Wojciechowski, K.; Górski, Ł.; Ciosek-Skibińska, P. Toward an Electronic Tongue Based on Surfactant-Stabilized Chemosensory Microparticles with a Dual Detection Mode. *ACS Appl. Mater. Interfaces* **2022**, *14* (44), 50375−50385.

(7) Toko, K. A Taste Sensor. *Meas. Sci. Technol.* **1998**, *9* (12), 1919−1936.

(8) Yeom, J.; Choe, A.; Lim, S.; Lee, Y.; Na, S.; Ko, H. Soft and Ion-Conducting Hydrogel Artificial Tongue for Astringency Perception. *Sci. Adv.* **2020**, *6* (23), 1−8.

(9) Shimizu, F. M.; Pasqualeti, A. M.; Todão, F. R.; De Oliveira, J. F. A.; Vieira, L. C. S.; Gonçalves, S. P. C.; Da Silva, G. H.; Cardoso, M. B.; Gobbi, A. L.; Martinez, D. S. T.; Oliveira, O. N.; Lima, R. S. Monitoring the Surface Chemistry of Functionalized Nanomaterials with a Microfluidic Electronic Tongue. *ACS Sens.* **2018**, *3* (3), 716−726.

(10) Han, J. K.; Park, S. C.; Yu, J. M.; Ahn, J. H.; Choi, Y. K. A Bioinspired Artificial Gustatory Neuron for a Neuromorphic Based Electronic Tongue. *Nano Lett.* **2022**, *22* (13), 5244−5251.

(11) Kim, H. J.; Lee, C. W.; Park, S.; Choi, S.; Park, S. H.; Nam, G. B.; Ryu, J. El; Eom, T. H.; Kim, B.; Kim, C. J.; Kim, S. Y.; Jang, H. W. MXene-Based High Performance Microfluidic PH Sensors for Electronic Tongue. *Sensors Actuators B Chem.* **2024**, *409*, 135636.

(12) Winquist, F. Voltammetric Electronic Tongues - Basic Principles and Applications. *Microchim. Acta* **2008**, *163* (1−2), 3−10.

(13) Podrazka, M.; Baczynska, E.; Kundys, M.; Jelen, P.; Witkowska Nery, E. Electronic Tongue-A Tool for All Tastes? *Biosensors* **2018**, *8*, 3−24.

(14) Aliev, T. A.; Belyaev, V. E.; Pomytkina, A. V.; Nesterov, P. V.; Shityakov, S.; Sadovnichii, R. V.; Novikov, A. S.; Orlova, O. Y.; Masalovich, M. S.; Skorb, E. V. Electrochemical Sensor to Detect Antibiotics in Milk Based on Machine Learning Algorithms. *ACS Appl. Mater. Interfaces* **2023**, *15* (44), 52010−52020.

(15) Zhu, L.; Sun, H.; Ma, M.; Mu, T. Utilization of Lacticaseibacillus Rhamnosus and Pediococcus Pentosaceus Cofermentation on Potato for Juice and High-Fiber Powder Production: An Innovative Approach for Pilot Scale Manufacturing. *ACS Food Sci. Technol.* **2024**, *4* (11), 2724−2738.

(16) Rudnitskaya, A.; Ehlert, A.; Legin, A.; Vlasov, Y.; Büttgenbach, S. Multisensor System on the Basis of an Array of Non-Specific Chemical Sensors and Artificial Neural Networks for Determination of Inorganic Pollutants in a Model Groundwater. *Talanta* **2001**, *55* (2), 425−431.

(17) de Morais, T. C. B.; Rodrigues, D. R.; de Carvalho Polari Souto, U. T.; Lemos, S. G. A Simple Voltammetric Electronic Tongue for the Analysis of Coffee Adulterations. *Food Chem.* **2019**, *273*, 31−38.

(18) Baldwin, E. A.; Bai, J.; Plotto, A.; Dea, S. Electronic Noses and Tongues: Applications for the Food and Pharmaceutical Industries. *Sensors* **2011**, *11* (5), 4744−4766.

(19) Akbar, M. A.; Selvaganapathy, P. R.; Kruse, P. Continuous Monitoring of Monochloramine in Water, and Its Distinction from Free Chlorine and Dichloramine Using a Functionalized Graphene-Based Array of Chemiresistors. *ACS ES T Water* **2024**, *4* (9), 4041−4051.

(20) Ben Jaballah, M.; Cetó, X.; Dridi, C.; Prieto-Simón, B. Voltammetric Electronic Tongue for the Discrimination of Antibiotic Mixtures in Tap Water. *J. Environ. Chem. Eng.* **2024**, *12* (5), 113831.

(21) Wang, M.; Cetó, X.; Del Valle, M. A Sensor Array Based on Molecularly Imprinted Polymers and Machine Learning for the Analysis of Fluoroquinolone Antibiotics. *ACS Sens.* **2022**, *7* (11), 3318−3325.

(22) Krieser, K.; Emanuelli, J.; Daudt, R. M.; Bilatto, S.; Willig, J. B.; Guterres, S. S.; Pohlmann, A. R.; Buffon, A.; Correa, D. S.; Külkamp-Guerreiro, I. C. Taste-Masked Nanoparticles Containing Saquinavir for Pediatric Oral Administration. *Mater. Sci. Eng., C* **2020**, *117* (July), 111315.

(23) Zhang, X.; Zhang, J.; Cai, Y.; Xu, S.; Wu, H.; Chen, X.; Huang, Y.; Li, F. Integrated Electrochemical Aptasensor Array toward Monitoring Anticancer Drugs in Sweat. *Anal. Chem.* **2024**, *96* (12), 4997−5005.

(24) Zaim, O.; Diouf, A.; El Bari, N.; Lagdali, N.; Benelbarhdadi, I.; Ajana, F. Z.; Llobet, E.; Bouchikhi, B. Comparative Analysis of Volatile Organic Compounds of Breath and Urine for Distinguishing Patients with Liver Cirrhosis from Healthy Controls by Using Electronic Nose and Voltammetric Electronic Tongue. *Anal. Chim. Acta* **2021**, *1184*, 339028.

(25) Lee, J. H.; Kim, D.; Kim, G.; Han, J. H.; Jeong, H. H. Binding-Free Taste Visualization with Plasmonic Metasurfaces. *ACS Appl. Mater. Interfaces* **2024**, *16* (13), 16622−16629.

(26) Jeong, J. Y.; Cha, Y. K.; Ahn, S. R.; Shin, J.; Choi, Y.; Park, T. H.; Hong, S. Ultrasensitive Bioelectronic Tongue Based on the Venus Flytrap Domain of a Human Sweet Taste Receptor. *ACS Appl. Mater. Interfaces* **2022**, *14* (2), 2478−2487.

(27) Ha, D.; Sun, Q.; Su, K.; Wan, H.; Li, H.; Xu, N.; Sun, F.; Zhuang, L.; Hu, N.; Wang, P. Recent Achievements in Electronic Tongue and Bioelectronic Tongue as Taste Sensors. *Sensors Actuators, B Chem.* **2015**, *207* (PB), 1136−1146.

(28) Kovacs, Z.; Szöllosi, D.; Zaukuu, J. L. Z.; Bodor, Z.; Vitális, F.; Aouadi, B.; Zsom-Muha, V.; Gillay, Z. Factors Influencing the Long-Term Stability of Electronic Tongue and Application of Improved Drift Correction Methods. *Biosensors* **2020**, *10* (7), 74.

(29) Richardson, J. J.; Björnmalm, M.; Caruso, F. Technology-Driven Layer-by-Layer Assembly of Nanofilms. *Science (80-.).* **2015**, DOI: 10.1126/science.aaa2491.

(30) Riul, A.; Dantas, C. A. R.; Miyazaki, C. M.; Oliveira, O. N. Recent Advances in Electronic Tongues. *Analyst* **2010**, *135* (10), 2481−2495.

(31) Cheneler, D.; Bowen, J. Degradation of Polymer Films. *Soft Matter* **2013**, *9* (2), 344−358.

(32) Gu, X.; Guo, X.-B.; Li, W.-H.; Jiang, Y.-P.; Liu, Q.-X.; Tang, X.-G. High-Entropy Materials for Application: Electricity, Magnetism, and Optics. *ACS Appl. Mater. Interfaces* **2024**, *16*, 53372.

(33) Yang, B.; Liu, Y.; Lan, S.; Dou, L.; Nan, C. W.; Lin, Y. H. High-Entropy Design for Dielectric Materials: Status, Challenges, and Beyond. *J. Appl. Phys.* **2023**, DOI: 10.1063/5.0138877.

(34) Miracle, D. B.; Senkov, O. N. A Critical Review of High Entropy Alloys and Related Concepts. *Acta Mater.* **2017**, *122*, 448−511.

(35) Guo, S.; Hu, Q.; Ng, C.; Liu, C. T. More than Entropy in High-Entropy Alloys: Forming Solid Solutions or Amorphous Phase. *Intermetallics* **2013**, *41*, 96−103.

(36) Oses, C.; Toher, C.; Curtarolo, S. High-Entropy Ceramics. *Nat. Rev. Mater.* **2020**, *5* (4), 295−309.

(37) Sen, S.; Palabathuni, M.; Ryan, K. M.; Singh, S. High Entropy Oxides: Mapping the Landscape from Fundamentals to Future Vistas. *ACS Energy Lett.* **2024**, *9* (8), 3694−3718.

(38) Lewin, E. Multi-Component and High-Entropy Nitride Coatings - A Promising Field in Need of a Novel Approach. *J. Appl. Phys.* **2020**, DOI: 10.1063/1.5144154.

(39) Zhou, Z. H.; Liu, X.; Liu, B. H.; Wang, Y. F.; He, C. Y.; Gao, X. H. High-Entropy Boride HfZrTiTaMoB: Promising Materials for

Solar Selective Absorption Coatings in Photothermal Applications. *ACS Appl. Mater. Interfaces* **2024**, *16*, 65446.
(40) Ivanov, Y. F.; Prokopenko, N. A.; Petrikova, E. A.; Shugurov, V. V.; Teresov, A. D.; Tolkachev, O. S. Structure and Properties of Hard Nitride Coatings from a High-Entropy Alloy. *J. Surf. Investig.* **2022**, *16* (6), 1061−1068.
(41) He, C. Y.; Gao, X. H.; Yu, D. M.; Guo, H. X.; Zhao, S. S.; Liu, G. Highly Enhanced Thermal Robustness and Photothermal Conversion Efficiency of Solar-Selective Absorbers Enabled by High-Entropy Alloy Nitride MoTaTiCrN Nanofilms. *ACS Appl. Mater. Interfaces* **2021**, *13* (14), 16987−16996.
(42) Khan, N. A.; Akhavan, B.; Zhou, C.; Zhou, H.; Chang, L.; Wang, Y.; Liu, Y.; Bilek, M. M.; Liu, Z. High Entropy Nitride (HEN) Thin Films of AlCoCrCu0.5FeNi Deposited by Reactive Magnetron Sputtering. *Surf. Coat. Technol.* **2020**, *402*, 126327.
(43) Zhao, L.; Yi, M.; Zhang, C.; Shan, T.; Zhang, J.; Yang, D.; Wang, J.; Bai, Y.; Guo, Q.; Xu, C. Mechanical Property and Cutting Performance of SiCw Toughened (Hf0.2Nb0.2Ta0.2Ti0.2Zr0.2)N High-Entropy Nitride Ceramic Cutting Tools by Spark Plasma Sintering. *Ceram. Int.* **2025**, *51*, 13174.
(44) Braic, V.; Balaceanu, M.; Braic, M.; Vladescu, A.; Panseri, S.; Russo, A. Characterization of Multi-Principal-Element (TiZrNbHfTa)N and (TiZrNbHfTa)C Coatings for Biomedical Applications. *J. Mech. Behav. Biomed. Mater.* **2012**, *10*, 197−205.
(45) Kumar, P.; Avasthi, S. Diffusion Barrier with 30-Fold Improved Performance Using AlCrTaTiZrN High-Entropy Alloy. *J. Alloys Compd.* **2020**, *814*, 151755.
(46) Garg, R.; Gonuguntla, S.; Sk, S.; Iqbal, M. S.; Dada, A. O.; Pal, U.; Ahmadipour, M. Sputtering Thin Films: Materials, Applications, Challenges and Future Directions. *Adv. Colloid Interface Sci.* **2024**, *330* (May), 103203.
(47) Shu, R.; Lundin, D.; Xin, B.; Sortica, M. A.; Primetzhofer, D.; Magnuson, M.; Le Febvrier, A.; Eklund, P. Influence of Metal Substitution and Ion Energy on Microstructure Evolution of High-Entropy Nitride (TiZrTaMe)N1- x(Me = Hf, Nb, Mo, or Cr) Films. *ACS Appl. Electron. Mater.* **2021**, *3* (6), 2748−2756.
(48) Jimenez, M. J. M.; Leidens, L. M.; Boeira, C. D.; Antunes, V. G.; Cemin, F.; Riul, A.; Zagonel, L. F.; Figueroa, C. A.; Wisnivesky, D.; Zanatta, A. R.; Alvarez, F. Experimental and Theoretical Insights on the Influence of Substrate Oscillation Period on Advanced Coatings Deposited by Dynamic Glancing Angle Deposition. *J. Mater. Res.* **2025**, *40*, 278.
(49) Shu, R.; Paschalidou, E. M.; Rao, S. G.; Lu, J.; Greczynski, G.; Lewin, E.; Nyholm, L.; le Febvrier, A.; Eklund, P. Microstructure and Mechanical, Electrical, and Electrochemical Properties of Sputter-Deposited Multicomponent (TiNbZrTa)Nx Coatings. *Surf. Coat. Technol.* **2020**, *389*, 125651.
(50) Honnali, S. K.; Poterie, C.; le Febvrier, A.; Lundin, D.; Greczynski, G.; Eklund, P. Effect of Tilted Closed-Field Magnetron Design on the Microstructure and Mechanical Properties of TiZrNbTaN Coatings. *J. Vac. Sci. Technol. A* **2023**, DOI: 10.1116/6.0002752.
(51) Cemin, F.; Luís Artico, L.; Piroli, V.; Andrés Yunes, J.; Alejandro Figueroa, C.; Alvarez, F. Superior in Vitro Biocompatibility in NbTaTiVZr(O) High-Entropy Metallic Glass Coatings for Biomedical Applications. *Appl. Surf. Sci.* **2022**, *596* (May), 153615.
(52) Cemin, F.; de Mello, S. R. S.; Figueroa, C. A.; Alvarez, F. Influence of Substrate Bias and Temperature on the Crystallization of Metallic NbTaTiVZr High-Entropy Alloy Thin Films. *Surf. Coat. Technol.* **2021**, *421*, 127357.
(53) Fairley, N.; Fernandez, V.; Richard-Plouet, M.; Guillot-Deudon, C.; Walton, J.; Smith, E.; Flahaut, D.; Greiner, M.; Biesinger, M.; Tougaard, S.; Morgan, D.; Baltrusaitis, J. Systematic and Collaborative Approach to Problem Solving Using X-Ray Photoelectron Spectroscopy. *Appl. Surf. Sci. Adv.* **2021**, *5* (June), 100112.
(54) Briggs, D.; Seah, M. P. *Pratical Surface Analysis*, 2nd ed.; Briggs, D., Seah, M. P., Eds.; John Wiley & Sons, Ltd: Chichester, UK, 1990; Vol. *1*.
(55) Shimizu, F. M.; Braunger, M. L.; Riul, A. Heavy Metal/Toxins Detection Using Electronic Tongues. *Chemosensors*; MDPI Multidisciplinary Digital Publishing Institute; 2019; pp 1−19. DOI: 10.3390/CHEMOSENSORS7030036.
(56) Riul, A.; de Barros, A.; Gaal, G.; Braunger, M. L.; Martinez Jimenez, M. J.; Avila-Avendano, C.; Rodrigues, V.; de Andrade, M. J.; Quevedo-Lopez, M.; Alvarez, F.; Baughman, R. H. Self-Healing E-tongue. *ACS Appl. Mater. Interfaces* **2023**, *15* (47), 55073−55081.
(57) Braunger, M. L.; Neto, M. P.; Kirsanov, D.; Fier, I.; Amaral, L. R.; Shimizu, F. M.; Correa, D. S.; Paulovich, F. V.; Legin, A.; Oliveira, O. N.; Riul, A. Analysis of Macronutrients in Soil Using Impedimetric Multisensor Arrays. *ACS Omega* **2024**, *9* (31), 33949−33958.
(58) Braunger, M. L.; Fier, I.; Shimizu, F. M.; de Barros, A.; Rodrigues, V.; Riul, A. Influence of the Flow Rate in an Automated Microfluidic Electronic Tongue Tested for Sucralose Differentiation. *Sensors (Switzerland)* **2020**, *20* (21), 6194.
(59) Varmuza, K.; Lohninger, H. 3 Principal Component Analysis of Chemical Data. *PCs for chemists* **1990**, *5*, 43−64.
(60) Otto, M. *Chemometrics*; Wiley, 2016; Vol. *11*. DOI: 10.1002/9783527699377.
(61) Cemin, F.; Luís Artico, L.; Piroli, V.; Andrés Yunes, J.; Alejandro Figueroa, C.; Alvarez, F. Superior in Vitro Biocompatibility in NbTaTiVZr(O) High-Entropy Metallic Glass Coatings for Biomedical Applications. *Appl. Surf. Sci.* **2022**, *596*, 153615.
(62) Huang, P. K.; Yeh, J. W. Effects of Nitrogen Content on Structure and Mechanical Properties of Multi-Element (AlCrNbSiTiV)N Coating. *Surf. Coat. Technol.* **2009**, *203* (13), 1891−1896.
(63) Sarkar, J. *Sputtering and Thin Film Deposition*; 2014; Vol. *2*, p 93..
(64) Liu, S.; Liu, C.; Yang, Z.; He, L.; Zeng, G.; Zhang, W.; Long, J.; Chang, H. Microstructure, High-Temperature Corrosion Resistance and Oxidation Properties of (TiVZrCrAl)N High Entropy Nitride Coatings with Different N2/Ar Ratios. *Surf. Coat. Technol.* **2024**, *476*, 130226.
(65) Huang, P. K.; Yeh, J. W. Effects of Substrate Temperature and Post-Annealing on Microstructure and Properties of (AlCrNbSiTiV)N Coatings. *Thin Solid Films* **2009**, *518* (1), 180−184.
(66) Zheng, J.; Zhang, C.; Li, J.; Chen, J.; Dong, Y.; Zhang, S.; Zhang, J.; Sun, D. (AlCrNiTiZr)Nx High-Entropy Nitride Coatings with Enhanced Hardness via Tailoring N2 Flow Rates for Anti-Wear Applications. *J. Vac. Sci. Technol. A* **2023**, DOI: 10.1116/6.0002837.
(67) Abadias, G. Stress and Preferred Orientation in Nitride-Based PVD Coatings. *Surf. Coat. Technol.* **2008**, *202* (11), 2223−2235.
(68) Zhang, X.; Jia, B.; Zeng, Z.; Zeng, X.; Wan, Q.; Pogrebnjak, A.; Zhang, J.; Pelenovich, V.; Yang, B. Machine Learning-Based Design of Superhard High-Entropy Nitride Coatings. *ACS Appl. Mater. Interfaces* **2024**, *16* (28), 36911−36922.
(69) Pshyk, A. V.; Vasylenko, A.; Bakhit, B.; Hultman, L.; Schweizer, P.; Edwards, T. E. J.; Michler, J.; Greczynski, G. High-Entropy Transition Metal Nitride Thin Films Alloyed with Al: Microstructure, Phase Composition and Mechanical Properties. *Mater. Des.* **2022**, *219*, 110798.
(70) Greczynski, G.; Primetzhofer, D.; Lu, J.; Hultman, L. Core-Level Spectra and Binding Energies of Transition Metal Nitrides by Non-Destructive x-Ray Photoelectron Spectroscopy through Capping Layers. *Appl. Surf. Sci.* **2017**, *396*, 347−358.
(71) Moulder, J. F.; Chastain, J. *Handbook of X-Ray Photoelectron Spectroscopy: A Reference Book of Standard Spectra for Identification and Interpretation of XPS Data*; Physical Electronics Division, Perkin-Elmer Corporation, 1992.
(72) Smidt, F. A. Use of Ion Beam Assisted Deposition to Modify the Microstructure and Properties of Thin Films. *Int. Mater. Rev.* **1990**, *35* (1), 61−128.
(73) De Maesschalck, R.; Jouan-Rimbaud, D.; Massart, D. L. The Mahalanobis Distance. *Chemom. Intell. Lab. Syst.* **2000**, *50* (1), 1−18.
(74) Struyf, A.; Hubert, M.; Rousseeuw, P. J. Clustering in an Object-Oriented Environment. *J. Stat. Softw.* **1996**, *1*, 1−30.
(75) Roper, S. D. Taste: Mammalian Taste Bud Physiology. *Curated Ref. Collect. Neurosci. Biobehav. Psychol.* **2017**, 887−893.